A Combined effect of the Earth's magnetic dipole tilt and IMF B_y in controlling auroral electron precipitation

J. Laitinen[1], L. Holappa[1], H. Vanhamäki[1]

[1]Space Physics and Astronomy Research Unit, University of Oulu, Oulu, Finland.

Key Points:

- IMF B_y and Earth's dipole tilt angle Ψ (season) modulate auroral electron precipitation
- Precipitation is stronger for 13.9-30 keV at auroral latitudes on the dawnside for both hemispheres, when B_y and Ψ have opposite signs
- B_y drives a strong dawn-dusk difference for energies 1.4-6.5 keV in the summer hemisphere

Corresponding author: J. Laitinen, `jussi.laitinen@oulu.fi`

Abstract

Precipitation of auroral electrons is usually assumed to be symmetric with respect to the sign of the dawn-dusk (B_y) component of the interplanetary magnetic field (IMF). This is also the case in most currently used precipitation models, which parameterize solar wind driving by empirical coupling functions. However, recent studies have showed that geomagnetic activity is significantly modulated by the signs and amplitudes of IMF B_y and the Earth's dipole tilt angle Ψ. This so called explicit B_y dependence is not yet included in any current precipitation models. In this paper, we quantify this B_y dependence for auroral electron precipitation for the first time. We use precipitation measurements of the Defense Meteorological Satellite Program (DMSP) Special Sensor J instruments from years 1995-2022. We show that the dawnside electron precipitation at energies 13.9-30 keV is greater at auroral latitudes for opposite signs of B_y and Ψ in both hemispheres, while the dusk sector is mostly unaffected by B_y and Ψ. For energies below 6.5 keV the B_y dependence is strong poleward of the auroral oval in the summer hemisphere, also exhibiting a strong dawn-dusk asymmetry. We also show that B_y dependence of precipitation modulates ionospheric conductance, which has important implications for solar wind response of ionospheric currents.

Plain Language Summary

Electron precipitation into the Earth's ionosphere creating the aurora borealis is driven by the magnetic field carried by the solar wind. The electron precipitation is known to increase the most, when the magnetic field of the solar wind points to south. The currently used models assume equally strong electron precipitation for eastward and westward solar wind magnetic fields. However, in this paper we show that the electron precipitation is different for duskward and dawnward magnetic fields, and that this magnetic field dependence varies with the season. We show that the electron precipitation is stronger on the dawnside in both hemispheres during the northern hemisphere winter when the solar wind magnetic field points duskward. In northern hemisphere summer the dependence on the magnetic field direction is opposite. We show that the solar wind magnetic field modulates the ionospheric conductivity in a similar way which has implications for ionospheric electric currents and related space weather effects on ground, such as disturbances on power lines.

1 Introduction

Space weather is driven by the solar wind and the interplanetary magnetic field (IMF) driving magnetic reconnection on the dayside magnetopause. This reconnection produces magnetospheric convection [*Dungey*, 1961], leading to geomagnetic activity and modulation of magnetospheric plasma populations. Accurate modelling of space weather has multiple benefits from both societal and scientific standpoints. One great challenge of space weather modelling is to accurately model auroral particle precipitation into the ionosphere which, together with the solar illumination, is the main driver of ionospheric conductance and thus fundamentally important for ionospheric dynamics.

Hardy et al. [1985] developed the first statistical precipitation model based on Defense Meteorological Satellite Program (DMSP) Special Sensor J (SSJ) data. The Hardy model is parameterized by the geomagnetic Kp index. As the DMSP particle data set has grown over the years, new models have followed [*Newell et al.*, 2009; *Zhu et al.*, 2021]. One example is the widely used OVATION auroral precipitation model [*Newell et al.*, 2014], which also takes into account seasonal variation and effects of different types of aurora. Instead of the discrete Kp index, the OVATION model is parametrized by the Newell coupling function [*Newell et al.*, 2007]

$$d\Phi/dt = v^{4/3} B_T^{2/3} \sin^{8/3}(\theta/2), \tag{1}$$

where v is the solar wind speed, $B_T = \sqrt{B_z^2 + B_y^2}$ and $\theta = \text{arctan2}(B_y/B_z)$ is the so-called clock angle.

The Newell coupling function has similarities to other existing coupling functions, predicting enhanced coupling with enhanced v and north-south (B_z) component. While the dawn-dusk component (B_y) is also included, its effect is symmetric with respect to its sign. That is, the OVATION model predicts equally strong precipitation for positive and negative IMF B_y. However, a considerable amount of research has shown that the sign of the IMF B_y component has an important effect in magnetospheric convection [*Cowley*, 1981; *Chisham et al.*, 2007; *Tenfjord et al.*, 2015] and in geomagnetic activity, which is more prominent during periods of high dipole tilt Ψ (90° minus the angle between the Earth's magnetic dipole axis and the Sun-Earth line). In geomagnetic activity, this effect can be summarized with a following rule: particle precipitation and geomagnetic activity are increased, when IMF B_y and Ψ have opposite signs [*Holappa et al.*, 2020; *Reis-*

tad et al., 2020; *Ohma et al.*, 2021]. This so-called explicit B_y-effect has been shown to modulate the westward electrojet [*Friis-Christensen and Wilhjelm*, 1975; *Friis-Christensen et al.*, 2017; *Holappa and Mursula*, 2018], size of the polar cap [*Reistad et al.*, 2020], and the substorm occurrence rate [*Ohma et al.*, 2021]. All above studies have found B_y-effects following the same rule, suggesting that the above effects are connected via similar physical mechanism.

Holappa et al. [2020] studied the explicit B_y dependence in energetic electron precipitation in both hemispheres using the National Oceanic and Atmospheric Administration (NOAA) Polar-Orbiting Operational Environmental Satellites. They found that energetic (>30 keV) electron precipitation is modulated by the IMF B_y component. In NH winter (negative Ψ) the flux of precipitating electrons is greater for positive B_y than for negative B_y in both hemispheres. In NH summer (positive Ψ), the B_y dependence is reversed. The effect was found to be strong in the midnight and dawn sectors and weak in the dusk sector. Also, the magnitude of the B_y-effect was found to be roughly equal in both hemispheres and solstices. If also auroral electrons (1-30 keV) would be modulated by IMF B_y in a similar way, the B_y dependence would also be significant for ionospheric conductance. However, the B_y dependence of auroral electron precipitation has not been yet studied directly. Nevertheless, statistical studies of field-aligned currents (FACs) have provided some indirect evidence [*Anderson et al.*, 2008; *Green et al.*, 2009; *Laundal et al.*, 2018; *Holappa et al.*, 2021; *Workayehu et al.*, 2021], because the upward FACs are known to be related to electron precipitation [e.g., *Korth et al.*, 2014].

None of the current precipitation models are designed to take the possible seasonally dependent B_y-effect in auroral particle precipitation into account. The recently developed ASHLEY precipitation model [*Zhu et al.*, 2021] uses the sign of the IMF B_y component as an input, but does not include seasonal dependence, which is crucial for B_y-effects. A machine-learning precipitation model by *McGranaghan et al.* [2021] includes B_y as an input, but its effect on precipitation patterns has not been quantified.

The goal of this paper is to quantify the possible explicit IMF B_y dependence of auroral (1-30 keV) electron precipitation, especially during periods of large dipole tilt. We also quantify the B_y dependence on ionospheric conductance and discuss its implications to geomagnetic activity. This is done by utilizing the database of DMSP SSJ particle data from years 1995-2022, which is also the basis for several existing precipitation models.

This paper is organized as follows. In Section 2 we present the general properties of the DMSP satellites and their instruments measuring the precipitating particles, and go through the data processing techniques forming the results. In Section 3 we show the B_y-effect in the measured differential number flux and in the calculated total energy flux and average energy. Also, we show the B_y-effect in the calculated Hall conductance. In Section 4 we discuss how the results affect the modern precipitation models, and how the results compare to the recent literature of the B_y-effect. Finally we present our conclusions in Section 5.

2 Data and Methods

2.1 DMSP Particle Data

In this study we use DMSP particle data from years 1995-2022, from DMSP satellites F10 through F19 (with F19 covering only years 2014-2016). DMSP satellites fly in circular, sun-synchronous polar orbits (inclination 98.8°) at an altitude of roughly 850 km. The orbits are predominantly confined to the dawn-dusk sector. However, the satellites jointly cover most magnetic local times (MLTs) at high geomagnetic latitudes (MLAT) in altitude adjusted corrected geomagnetic (AACGM) coordinates, but the MLT-MLAT coverage has hemispheric differences, due to hemispheric differences in the structure of the Earth's magnetic field. The satellites carry a Special Sensor for Precipitating Particles versions 4 (SSJ/4) and 5 (SSJ/5) that measure fluxes of downward precipitating auroral electrons and ions [*Hardy et al.*, 2008; *Redmon et al.*, 2017]. The SSJ/4 points upwards and measures electrons and ions with energies from roughly 30 eV to 30 keV in 19 logarithmically-spaced energy bins, resulting in full electron and ion spectra every second. SSJ/4 instruments are used in this study with satellites F10-F15. The SSJ/5 instrument is an updated version of SSJ/4. The difference is that it measures the incoming flux of particles from a range of angles (from 4° to 90°), divided into six 15° angular sectors. However, due to constraints in telemetry, the counts from different angular sectors are averaged, resulting one spectrum every second (similarly as in SSJ/4). Due to these instrumental differences, there may by some systematic differences between the fluxes measured by SSJ/4 and SSJ/5. For instance, the larger field of view of the SSJ/5

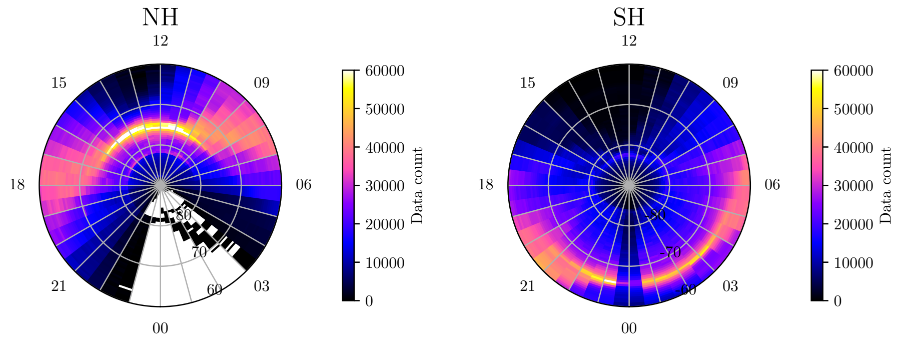

Figure 1. Data count of DMSP particle measurements from years 1995-2022 for northern (NH) and southern hemispheres (SH) after sorting the data with the criteria: IMF $|B_y| > 2$ nT, the Earth's dipole tilt angle $|\Psi| > 15°$, and the normalized Newell coupling function $1 < d\Phi/dt/\langle d\Phi/dt \rangle < 2$.

can result into measurement of electrons outside the loss cone, if the satellite is in the ascending phase [*Redmon et al.*, 2017]. However, the observed IMF B_y dependencies studied in this paper did not show systematic differences between SSJ/4 and SSJ/5, thus encouraging us to combine the data from both instruments to achieve the best possible data coverage. Also, the SSJ/4 and SSJ/5 data have been combined in previous studies [*Wing et al.*, 2013; *Newell et al.*, 2014; *McGranaghan et al.*, 2015]. All the satellites used in this study had the ascending nodes on the dusk side.

2.2 Data Processing

The DMSP particle measurements are spatially binned into an MLT-latitude grid with a grid size of 0.5 h MLT by 0.5° MLAT, from 60° to 90°. Figure 1 shows the data coverage of the DMSP measurements in the northern and southern hemispheres of the data used in this study. That is, after sorting the data with solar wind criteria IMF $|B_y| > 2$ nT and the normalized Newell coupling function $1 < d\Phi/dt/\langle d\Phi/dt \rangle < 2$ (see Section 3.1), and large Earth's dipole tilt angles $|\Psi| > 15°$.

Each MLT-MLAT bin contains the mean value of the differential number fluxes. Due to the heavy-tailed distribution of the differential particle flux, the mean is sometimes significantly affected by outliers. The effect of outliers is alleviated with the following automatic procedure. First, all the bins are checked for outliers by standardizing the differential number fluxes in the bin. The potential outliers are removed from the bin, if their standardized z-score is larger than 6σ and the value is larger than 10^4 $(1/\mathrm{cm}^2\mathrm{s}\cdot\mathrm{eV}\cdot\mathrm{sr})$. These criteria were found to eliminate most effects of outliers.

The total energy fluxes are calculated from the DMSP data from all of the 19 channels for each MLT-latitude bin from the outlier removed (first procedure) differential number fluxes. Total energy fluxes are calculated with equation [*Hardy et al.*, 2008]

$$
\begin{aligned}
JE_{TOT}(\Omega) =& E_1 j(E_1,\Omega)(E_2-E_1) + \sum_{i=2}^{18} E_i j(E_i,\Omega)\frac{E_{i+1}-E_{i-1}}{2} \\
&+ E_{19} j(E_{19},\Omega)(E_{19}-E_{18}),
\end{aligned}
\tag{2}
$$

where i is the channel index (from high to low), E_i is the channel central energy of channel i and $j(E_i,\Omega)$ is the directional-differential number flux (for further theoretical basis see, e.g., *Redmon et al.* [2017]). The total number fluxes $J_{TOT}(\Omega)$ are calculated in a similar manner, only replacing the $E_i j(E_i,\Omega)$ (directional-differential energy flux) term with $j(E_i,\Omega)$. The average energy for each bin is calculated as

$$
E_{AVE} = \frac{JE_{TOT}(\Omega)}{J_{TOT}(\Omega)}. \tag{3}
$$

Assuming isotropic pitch-angle distribution at DMSP altitude, we calculate the down-going total energy flux by multiplying $JE_{TOT}(\Omega)$ by π [*Newell et al.*, 2014]. The calculated down-going total energy flux and the average energy are used to calculate the Hall conductance for each bin using the Robinson formulas [*Robinson et al.*, 1987] to show the potential B_y-effect of auroral precipitation on ionospheric conductivity. The Robinson formulas are defined as

$$
\Sigma_P = \frac{40E_{AVE}}{16+(E_{AVE})^2}(JE_{TOT})^{1/2} \tag{4}
$$

$$
\frac{\Sigma_H}{\Sigma_P} = 0.45(E_{AVE})^{0.85}, \tag{5}
$$

where the Σ_P and Σ_H Pedersen and Hall conductances. The average energy E_{AVE} is in units of keV and the down-going total energy flux JE_{TOT} in ergs/cm^{2}s.

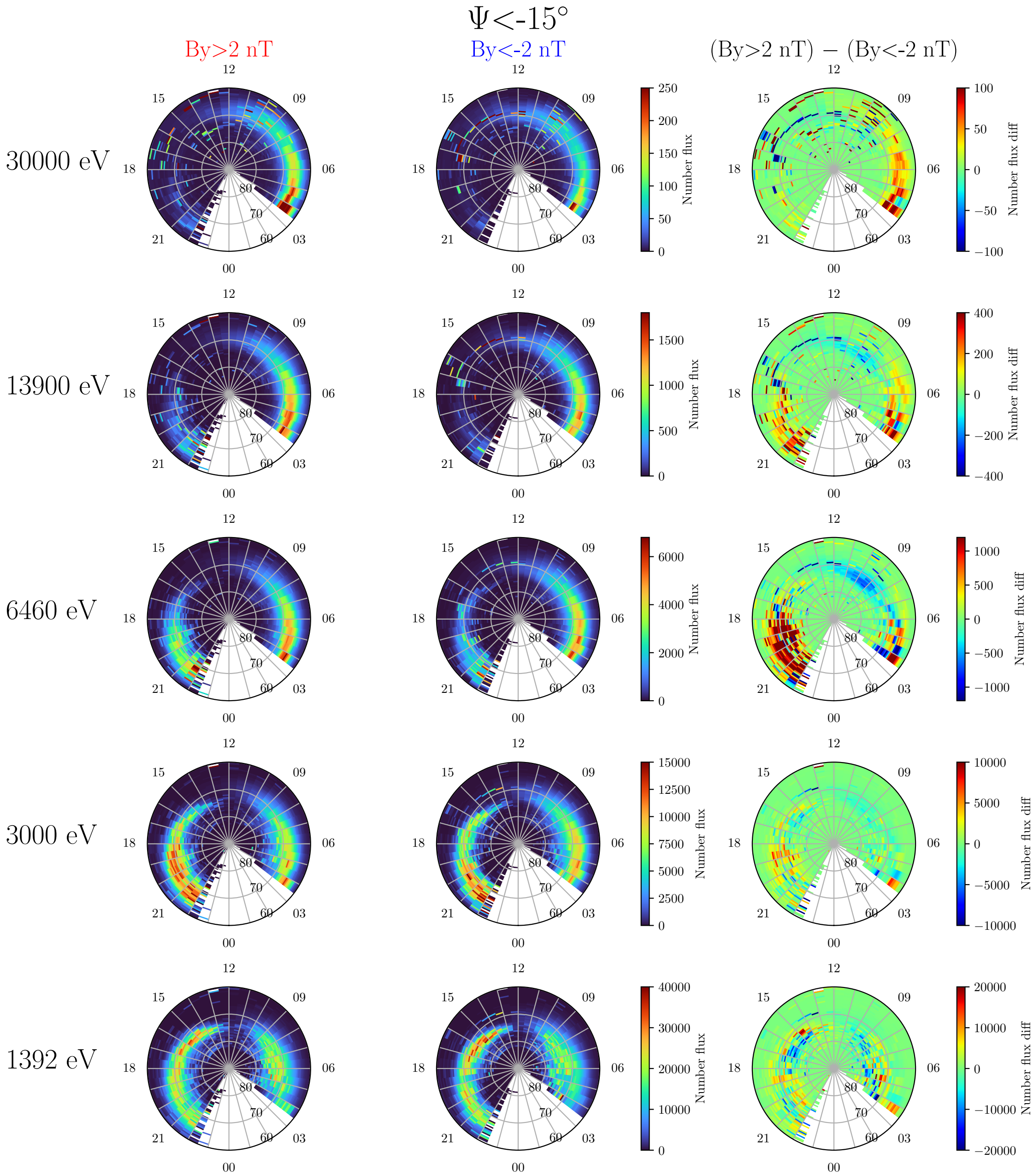

Figure 2. Precipitation map of the differential number fluxes ($1/\text{cm}^2\text{s} \cdot \text{eV} \cdot \text{sr}$) in the northern hemisphere with dipole tilt $\Psi < -15°$ (local winter) for five channels. The channel central energies are shown on the left for each row. The first two columns show the differential number fluxes, when the IMF $B_y > 2$ nT and $B_y < -2$ nT, and the third column shows the difference of these two precipitation maps. The maps cover MLATs from 60° to 90°. A large gap in data exists from 22 to 04 MLT.

3 Results

3.1 Differential number flux

For quantifying IMF B_y dependence of precipitation, we sort the DMSP data with IMF B_y and the Newell coupling function, averaged over the current and three previous UT hours. The Newell function is normalized by its mean $\langle d\Phi/dt \rangle$ in 1995-2022. Figure 2 shows a map of the differential number flux ($1/\mathrm{cm}^2\mathrm{s}\cdot\mathrm{eV}\cdot\mathrm{sr}$) in the northern hemisphere (NH) for dipole tilt $\Psi < -15°$ (local winter). In all panels the normalized Newell coupling function $d\Phi/dt/\langle d\Phi/dt \rangle$ is limited between 1 and 2. Thus, all panels correspond to solar wind driving slightly stronger than the long-term mean. Because the DMSP satellites are primarily on dawn-dusk orbits, there is no data coverage in the NH at 22-04 MLT and very limited data at 12-15 MLT between 60°-70° MLAT (see Figure 1). Each row displays a different energy channel labeled by nominal central energies of the channels. Precipitation maps are shown for five channels, showing every other channel starting from the highest channel (30 keV). Thus, to shorten the text, from here on out we reference these channels as 30 keV, 13.9 keV, 6.5 keV, 3 keV, and 1.4 keV. The first two columns show the differential number fluxes during positive ($>$ 2 nT) and negative B_y (< -2 nT), respectively, and the third column shows their difference. The first and second columns show that the amount of precipitation changes drastically between the energy channels. The precipitation patterns in the highest energy channels (30 keV and 13.9 keV) show strong dawn-dusk differences and the maximum precipitation region is located close to the auroral oval, while the lower channels show more dawn-dusk symmetric distributions, which extend poleward of the auroral oval.

Figure 2 (especially the third column) shows a clear B_y dependence for the highest energy channels (30 and 13.9 keV). The number fluxes are higher for $B_y > 2$ nT, especially on the dawnside auroral oval (at 60-70 MLAT). This effect can be seen in the 6.5 keV energy channel as well, but not as clearly. The 3 keV channel shows only weak B_y dependence and the 1.4 keV channel shows no systematic B_y-effect.

Figure 3 shows the precipitation map in NH for $\Psi > 15°$ (NH summer) in a similar format as Figure 2. The B_y dependence during positive tilt (quantified in the third column) is clearly opposite to that during negative tilt (Figure 2), in agreement with the earlier results on the B_y dependence of high energy precipitation [*Holappa et al.*, 2020]. The number fluxes are greater for $B_y < -2$ nT than for $B_y > 2$ nT on the dawn side

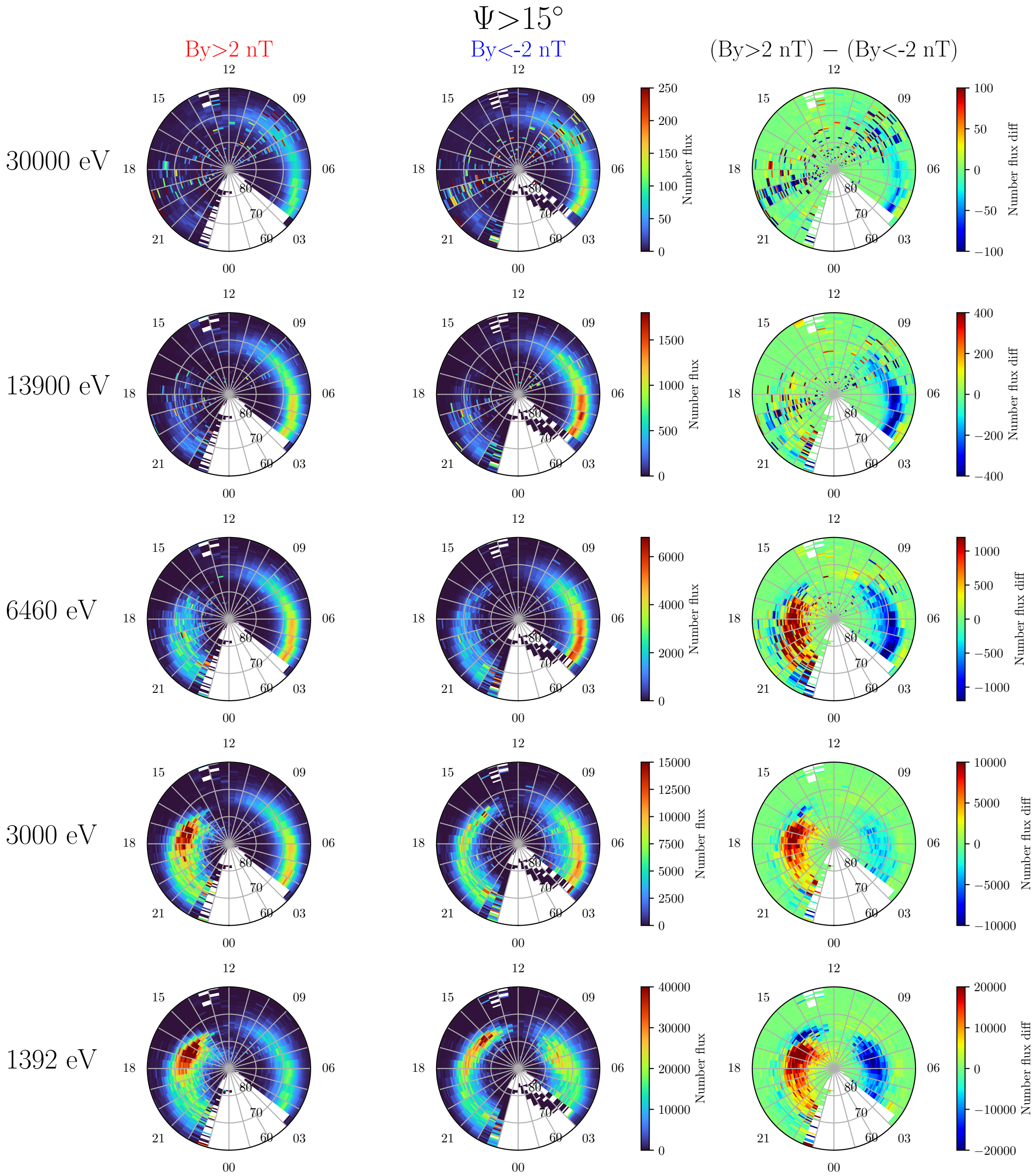

Figure 3. Precipitation map of the differential number fluxes ($1/\mathrm{cm}^2\mathrm{s}\cdot\mathrm{eV}\cdot\mathrm{sr}$) in the northern hemisphere with dipole tilt $\Psi > 15°$ (local summer) in similar format as in Figure 2.

in all channels. There are, however, also other differences between summer and in winter precipitation patterns: a strong dawn-dusk difference is seen in channels 6.5 keV, 3 keV and 1.3 keV, so that the number fluxes increase on the dawnside during $B_y < -2$ nT and on the duskside during $B_y > 2$ nT. The B_y-effect is seen to extend to higher latitudes with decreasing energies.

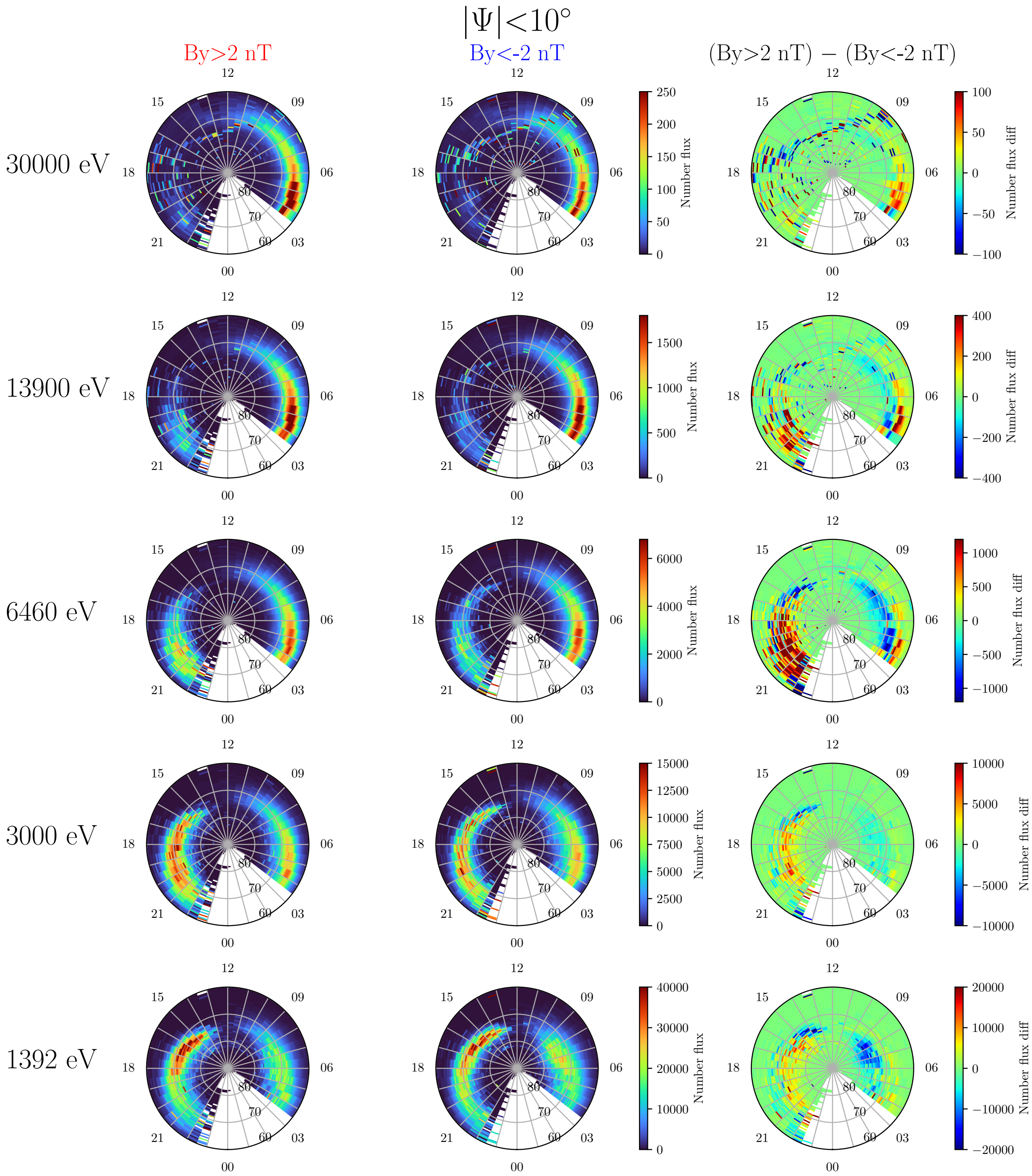

Figure 4. Precipitation map of the differential number fluxes ($1/\mathrm{cm}^2\mathrm{s}\cdot\mathrm{eV}\cdot\mathrm{sr}$) in the northern hemisphere with dipole tilt $|\Psi| < 10°$ (neutral tilt) in similar format as in Figure 2.

Figure 4 shows the precipitation map in NH for $|\Psi| < 10°$ (neutral tilt). The B_y dependence varies between the higher and lower channels. The 30 keV channel shows greater number fluxes for $B_y > 2$ nT at dawnside auroral latitudes similar to Figure 2, but weaker. However, channel 13.9 keV shows unclear B_y dependence on the dawnside, but greater number fluxes on the duskside for $B_y > 2$ nT. Channels 3 keV and

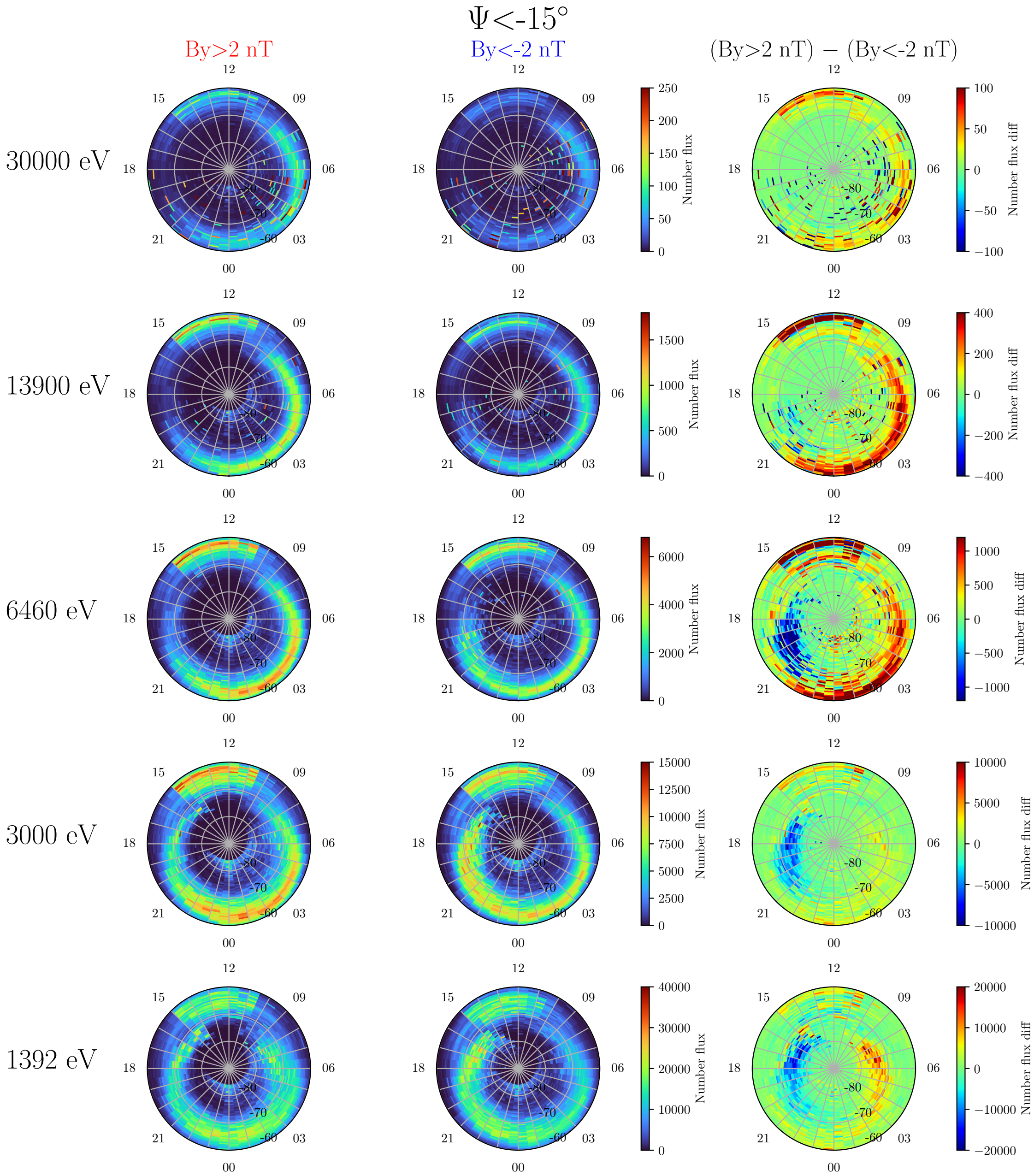

Figure 5. Precipitation map of the differential number fluxes ($1/\mathrm{cm}^2\mathrm{s}\cdot\mathrm{eV}\cdot\mathrm{sr}$) in the southern hemisphere with dipole tilt $\Psi < -15°$ (local summer) in similar format as in Figures 2-4.

1.4 keV display similar, but much weaker B_y dependence seen for NH summer in Figure 3.

Figure 5 shows the precipitation map of the differential number flux in the southern hemisphere (SH) with dipole tilt $\Psi < -15°$ (SH summer). The notable difference to the northern hemisphere (Figure 3) is the better MLT-MLAT coverage. However, the data coverage is poor at the dayside between 10-15 MLT (Figure 1), which produces clear anomalies in all panels. In the first two columns, channels from 6.5 keV to 30 keV show similar precipitation patterns maximizing at the auroral latitudes between 21 and 09 MLT. In the lower energy channels precipitation extends roughly from 17 MLT to 09 MLT. The third column shows a clear B_y dependence for energies between 6.5 keV and 30 keV. The number fluxes are clearly greater for $B_y > 2$ nT at 22-09 MLT. The effect is in the same direction as in the NH local summer, implying it is from the same, global physical mechanism. Channels between 1.4-6.5 keV show increased number fluxes in the duskside, and the channel 3 keV does not show as clear increase of dawnside number fluxes during $B_y > 2$ nT. The channel 1.4 keV shows a high latitude dawn-dusk difference, which is opposite and weaker to that in NH summer (Figure 3).

Figure 6 shows the precipitation map in SH during $\Psi > 15°$ (SH winter). The number fluxes are generally slightly larger overall than in SH summer (Figure 5). A B_y dependence is also seen in the highest energy channels (30 keV and 13.9 keV) at dawn and pre-midnight sectors, but it is weaker than in SH summer. Channels from 6.5 keV to 1.4 keV do not show a clear B_y-effect.

Comparing the above results from the two hemispheres we can summarize that at the dawn sector auroral latitudes precipitation increases for opposite signs of IMF B_y and Ψ in both hemispheres. However, the B_y dependence is stronger in the summer hemisphere. In the summer hemisphere IMF B_y drives a clear dawn-dusk asymmetry in high-latitude ($> 70°$) precipitation. This effect is most clear for the lowest energy (1.4 keV) for which the precipitation patterns during positive and negative B_y are almost mirror images of each other. This ”mirroring” is seen best in the SH (Figure 5), where the MLT coverage is better than in the NH.

To further quantify the B_y dependence in the NH at dawn, Figure 7 shows a meridional cut at 05-07 MLT of the differential number fluxes from Figures 2 and 3 together with their standard errors. The dawside precipitation shows larger number fluxes for $B_y > 2$ nT than for $B_y < -2$ nT for 30 keV during $\Psi < -15°$. However, 3 keV shows slightly larger number fluxes for $B_y < -2$ nT than for $B_y > 2$ nT. Other energies show only small or no clear B_y-effect. During $\Psi > 15°$ the number fluxes are larger and peak roughly 0.5° MLAT poleward for $B_y < -2$ nT than for $B_y > 2$ nT for energies between 6.5

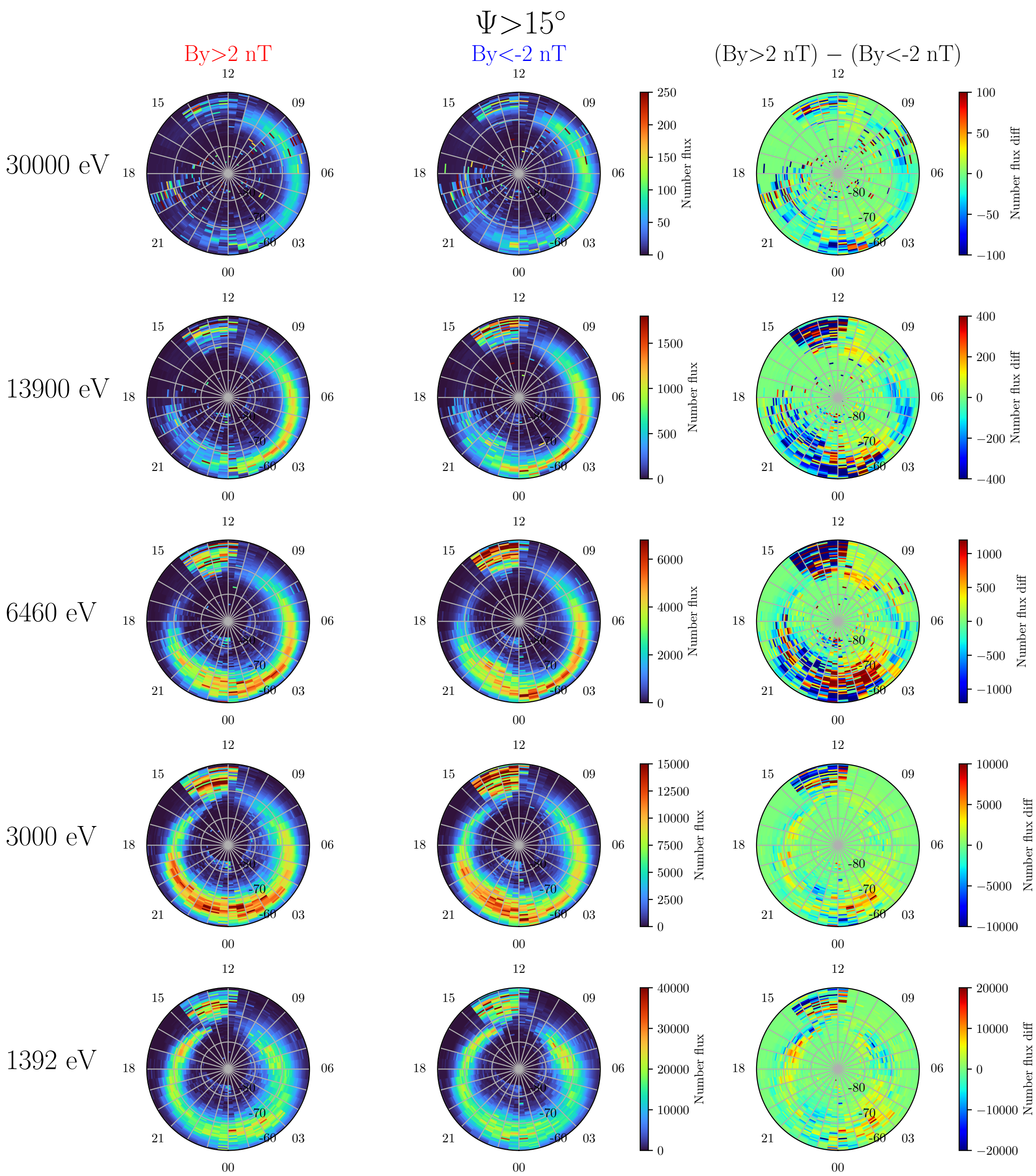

Figure 6. Precipitation map of the differential number fluxes ($1/\mathrm{cm}^2\mathrm{s}\cdot\mathrm{eV}\cdot\mathrm{sr}$) in the southern hemisphere with dipole tilt $\Psi > 15^\circ$ (local winter) in similar format as in Figures 2-6.

keV and 30 keV. Energies 1.4 keV and 3 keV show number fluxes extending to higher latitudes with decreasing energies. The number fluxes at dusk (17-19 MLT, Figure 8) show only slightly larger number fluxes for $B_y > 2$ nT than for $B_y < -2$ nT during $\Psi < -15^\circ$ for energies between 3 keV and 13.9 keV. However, during $\Psi > 15^\circ$ ener-

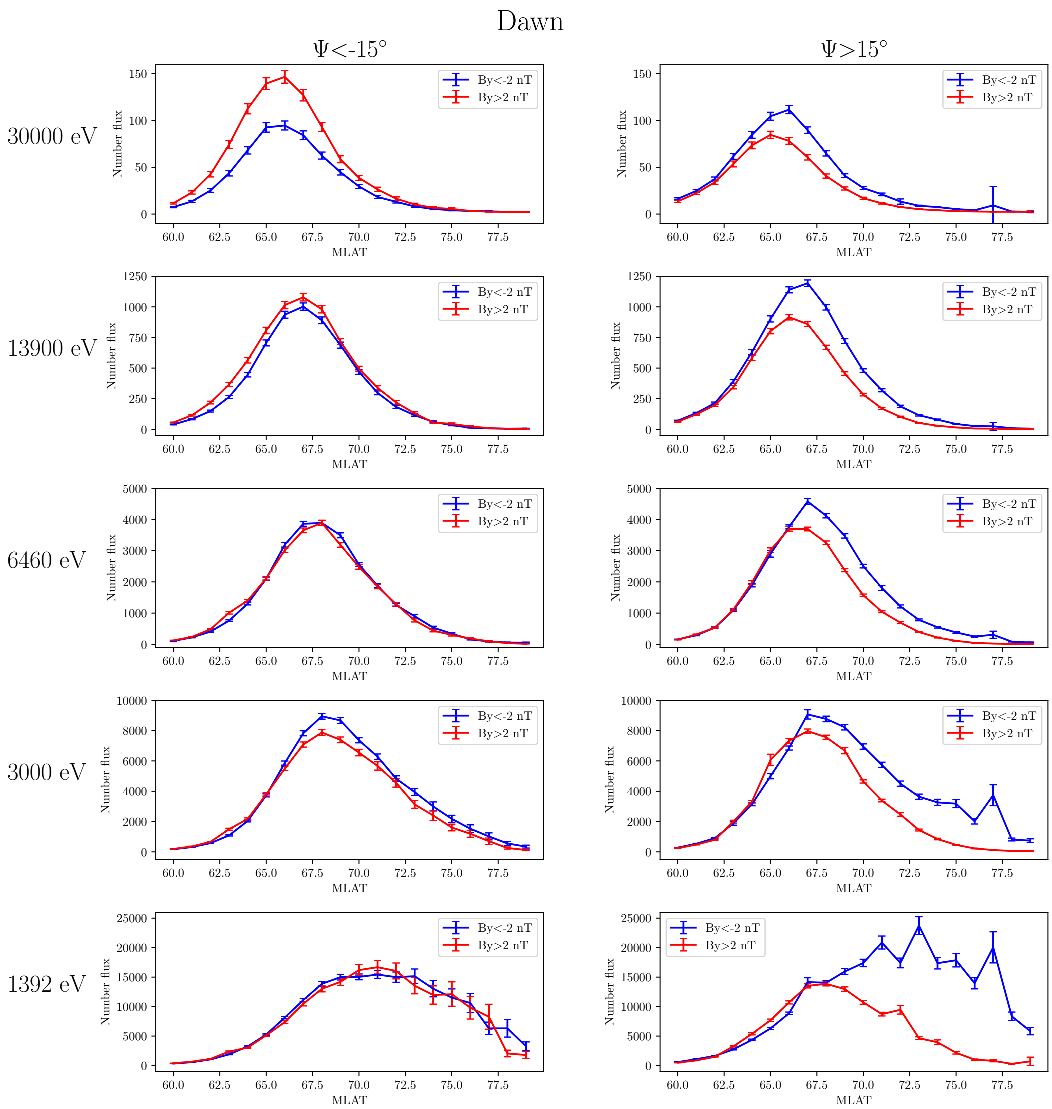

Figure 7. Northern hemisphere dawnside differential number fluxes ($1/\mathrm{cm}^2\mathrm{s}\cdot\mathrm{eV}\cdot\mathrm{sr}$) from sector 05-07 MLT shown with error bars for winter ($\Psi < -15°$) and summer ($\Psi > 15°$). Red line corresponds to number fluxes during IMF $B_y > 2$ nT and blue line during $B_y < -2$ nT.

gies from 1.4 keV and 6.5 keV show larger number fluxes that extend to higher latitudes for $B_y > 2$ nT than for $B_y < -2$.

In the calculation of the standard errors $\sigma/\sqrt{N}$ we used the number of orbits as the factor N. This ensures that we treat only measurements made during different orbits as statistically independent from each other. As seen in Figure 7, errorbars at the dawnside stay relatively small, indicating that the results are statistically reliable. However, Figure 8 shows much larger errorbars for 30 keV and 13.9 keV channels for both

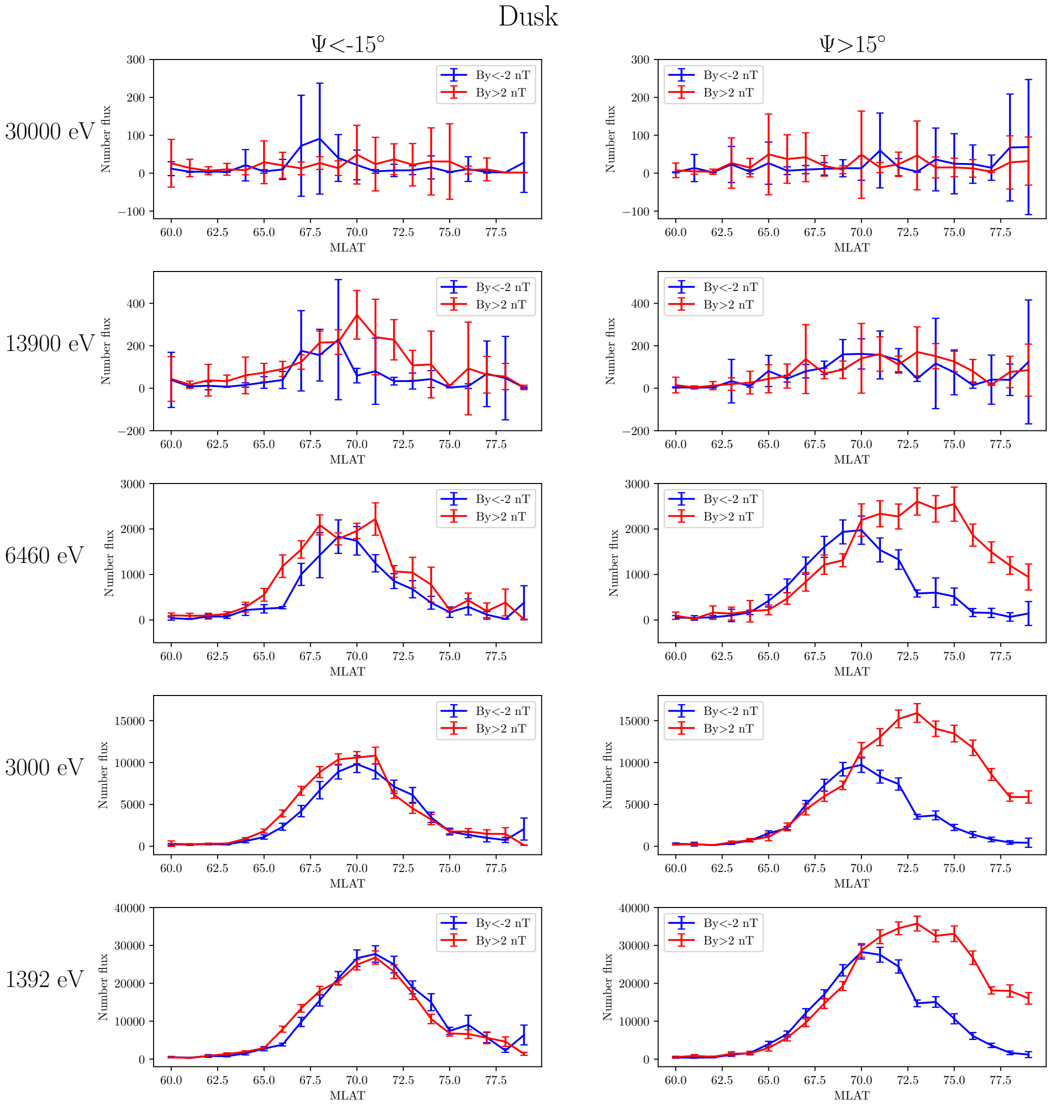

Figure 8. Northern hemisphere duskside differential number fluxes ($1/\mathrm{cm}^2\mathrm{s}\cdot\mathrm{eV}\cdot\mathrm{sr}$) from sector 17-19 MLT shown with error bars for summer ($\Psi > 15°$) and winter ($\Psi < -15°$). Red line corresponds to number fluxes during IMF $B_y > 2$ nT and blue line during $B_y < -2$ nT.

tilt angles at dusk, while 6.5 keV, 3 keV, and 1.4 keV channels show relatively small errorbars for both tilt angles, comparable to ones in the dawn side in Figure 7. Therefore, the relatively high uncertainties should be kept in mind when interpreting the high-energy part of dusk precipitation (30 keV and 13.9 keV) in Figures 2 and 3.

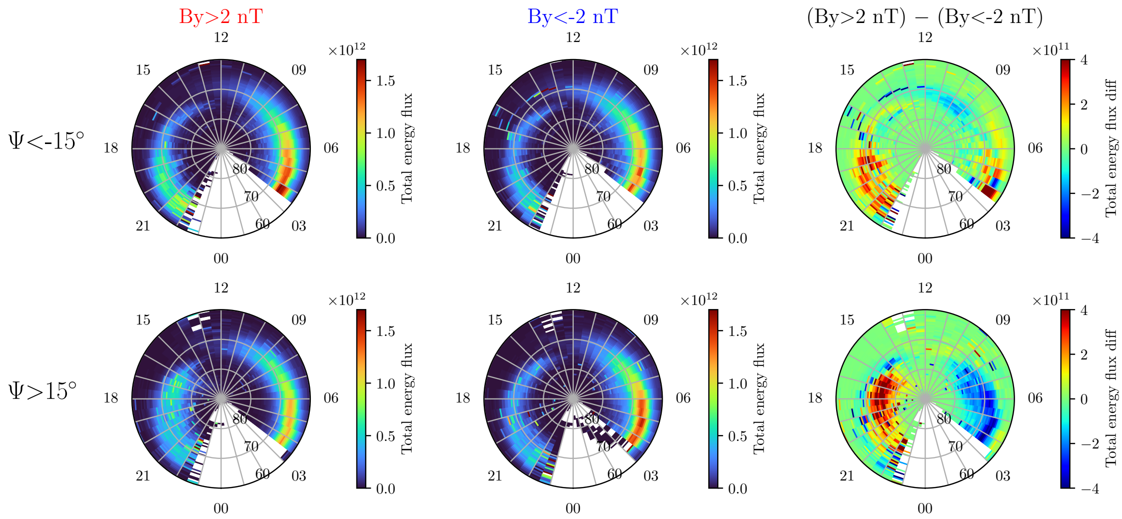

Figure 9. Total energy fluxes (eV/cm^{2}s $\cdot$ sr) for the northern hemisphere. The first row are the total energies for tilt angle $\Psi < -15°$ and the second row for tilt angle $\Psi > 15°$. First column shows the total energies for IMF $B_y > 2$ nT, second row for $B_y < -2$ nT, and the third row the difference of the two total energy flux maps.

3.2 Total energy flux, average energy and ionospheric conductivity

Figure 9 shows the total energy fluxes for the NH calculated with Equation (2) for $\Psi < -15°$ in the first row and $\Psi > 15°$ in the second in a similar format as Figures 1-4. Figure 9 shows similar B_y dependencies as Figures 2 and 3. During $\Psi < -15°$ the total energy fluxes are generally larger for IMF $B_y > 2$ at both dawn and dusk. However, for $\Psi > 15°$ IMF B_y drives a clear dawn-dusk asymmetry in energy fluxes with higher dawn (dusk) energy flux for $B_y < -2$ ($B_y > 2$) nT. The B_y-effect during $\Psi > 15°$ is seen at higher latitudes than for $\Psi < -15°$. This is due to the effect of Ψ onto the particle precipitation measured by the lower energy channels, as seen in Figure 3. Figure S1 in the Supplement shows the total energy fluxes for the SH in a similar format.

Figure 10 shows the average energy (eV) for the NH in a format similar to Figure 9. When the tilt angle Ψ and IMF B_y have opposite signs, the average energy increases on the dawnside. During $\Psi > 15°$, the average energies also only show weak dawn-dusk difference compared to Figure 9. Also, the average energy increases in only slightly higher

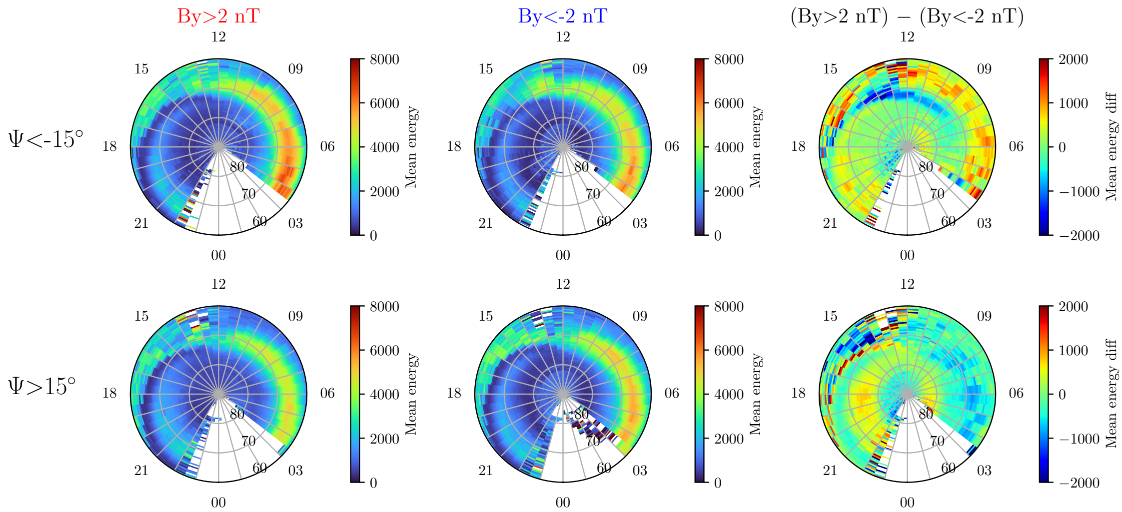

Figure 10. Average energies (eV) for the northern hemisphere, in a similar format as in Figure 9.

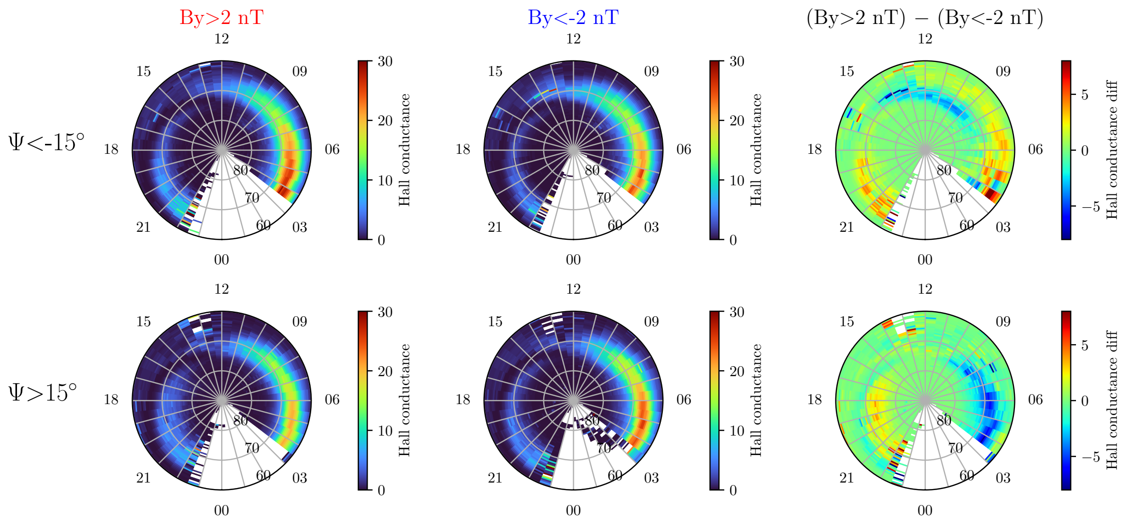

Figure 11. Calculated Hall conductances (S) for the northern hemisphere, in a similar format as in Figure 9 and 10. The conductances were calculated using the Robinson formulas.

latitudes in the duskside during $B_y > 2$ nT, than in the dawnside during $B_y < -2$ nT. Figure S2 in the Supplement shows the average energy for the SH.

The total energy flux and average energy are known to directly affect the ionospheric Hall and Pedersen conductances. This relation is described by the Robinson formulas given in Eqs. (4-5). Figure 11 shows the Hall conductances (in Siemens) calculated from the total energy flux and average energy, in a similar format as Figures 9 and 10. During $\Psi < -15°$ the Hall conductance is increased with $B_y > 2$ nT, similarly as the total energy flux and average energy in Figures 9 and 10. During $\Psi > 15°$ the Hall conductance is greater for $B_y < -2$ nT at dawn and for $B_y > 2$ nT at dusk. However, $\Psi > 15°$ shows only weak dawn-dusk difference between $B_y > 2$ nT and $B_y < -2$ nT. Also, as the B_y-effect in precipitation is seen in higher latitudes during $\Psi > 15°$ than during $\Psi < -15°$, the Hall conductance shows similar effect. Many studies have shown that the variability of the westward electrojet is mainly controlled by variations of the Hall conductance (rather than the electric field) [e.g., *Sugino et al.*, 2002; *Sergeev et al.*, 2018]. Therefore, the result here implies that the conductance would enhance the westward electrojet more during $\Psi > 15°$ and $B_y < -2$ nT, and during $\Psi < -15°$ and $B_y > 2$ nT.

4 Discussion

Figures 2-6 show that auroral electron precipitation at 1-30 keV energies clearly depends on the combination of IMF B_y direction and dipole tilt angle Ψ. We found that the energetic part (13.9-30 keV) of the auroral precipitation at the dawn sector is greater for opposite signs of IMF B_y and Ψ in both hemispheres, in a similar way as found in > 30 keV electrons in *Holappa et al.* [2020]. However, the B_y dependence of auroral electrons is more prominent in the summer hemisphere.

For less energetic part of auroral precipitation (below 6.5 keV) IMF B_y dependence is somewhat different. Figures 3 and 5 show a strong dawn-dusk asymmetry between positive and negative B_y poleward of the auroral oval in the summer hemisphere. This dawn-dusk difference is almost mirrored in the 1.4 keV precipitation patterns. In the NH, B_y is found to increase the dawnside precipitation for $B_y < -2$ nT and duskside for $B_y > 2$ nT. In the SH, this B_y-effect is seen in the opposite direction.

The dawnside (diffuse electron) precipitation is known to be mostly due to wave-particle interactions between electrons and whistler-mode waves resulting into pitch angle scattering of bouncing electrons [*Li et al.*, 2009; *Thorne et al.*, 2010]. However, also broadband accelerated electron precipitation is found to peak at prenoon [*Newell et al.*, 2009]. Whistler-mode waves are known to originate from non-isotropic 10-30 keV electrons injected into the inner magnetosphere during substorms [*Tsurutani and Smith*, 1974; *Li et al.*, 2010]. Also, substorms are known to increase the diffuse electron precipitation on the dawnside [*Wing et al.*, 2013]. Thus, it is probable that the IMF B_y modulates the energetic (13.9-30 keV) dawnside precipitation via occurrence rate of substorms, because substorm occurrence rate is found to show similar B_y dependence [*Ohma et al.*, 2021]. This is supported by Figure 10, which shows that the average energy of precipitating electrons increases on dawnside, probably due to injected energetic electrons by increased frequency of substorms.

The duskside precipitation is known to consist mostly of monoenergetic electrons, accelerated due to field-aligned potential differences [*Newell et al.*, 2009]. These accelerated electrons are known to be often confined within the upward (R1) FAC in the dusk-to-midnight sector [*Ohtani et al.*, 2010; *Korth et al.*, 2014]. The B_y dependence of these FACs has been studied in the past [*Weimer*, 2001; *Anderson et al.*, 2008; *Tenfjord et al.*, 2015; *Laundal et al.*, 2018; *Workayehu et al.*, 2021]. The duskside R1 FAC is known to shift and expand into higher latitudes for positive B_y in the NH summer and for negative B_y in the SH summer [*Green et al.*, 2009; *Holappa et al.*, 2021]. This is similar to the B_y-effect in the low-energy part ($<$ 6.5 keV) of duskside precipitation in Figures 3 and 5. The precipitation patterns of 1.4 keV electrons in the summer hemisphere for positive and negative IMF B_y are almost mirror images of each other, which could be explained by the dawn-dusk asymmetry of FACs due to asymmetric magnetospheric convection driven by IMF B_y [*Cowley*, 1981; *Tenfjord et al.*, 2015; *Reistad et al.*, 2021]. The B_y-effect in 1.4 keV electron precipitation seen in the summer hemisphere would then be explained by dawn or dusk magnetic field lines convecting at higher latitudes depending on the sign of B_y [*Tenfjord et al.*, 2015]. Enhanced conductivity due to increased solar illumination on these field lines in turn allow stronger FACs [*Green et al.*, 2009] (and thus particle precipitation). However, all different precipitation mechanisms are mixed in the statistical patterns derived in this paper. Therefore, without further studies we cannot make strong conclusions on how IMF B_y modulates different precipitation mechanisms, especially at low ($<$ 6 keV) energies.

We calculated the total energy flux and average energy of precipitating electrons and derived ionospheric conductances from these parameters using the Robinson formulas. Our results show that IMF B_y indeed affects the ionospheric conductance, especially in the dawn sector where the Hall conductance is greater for opposite signs of B_y and Ψ (the difference being about 5 Siemens during moderate solar wind driving $d\Phi/dt/\langle d\Phi/dt\rangle$). Similar results were found by *Weimer and Edwards* [2021] using an ionospheric data assimilation method, and by *Carter et al.* [2020] for the dayside NH summer Hall conductances using DMSP SSUSI measurements.

Our results contribute also toward understanding the physics behind IMF B_y dependence of the westward electrojet, which was found already by *Friis-Christensen and Wilhjelm* [1975] using ground magnetometers in Greenland. Later studies based on polar-orbiting satellites [*Friis-Christensen et al.*, 2017; *Smith et al.*, 2017; *Workayehu et al.*, 2021] and the AL index [*Holappa and Mursula*, 2018] have quantified this B_y dependence in more detail and found that the NH westward electrojet is about 40-50% stronger for negative tilt and positive IMF B_y. However, the NH westward electrojet shows a much weaker B_y dependence during positive tilt (NH summer). This summer-winter difference may be related to seasonal variation of ionospheric conductivity. The IMF B_y dependence of conductance (through particle precipitation) quantified above is relatively more significant in the dark winter hemisphere while in the summer hemisphere conductance is also affected by sunlight. The B_y dependence of conductance could explain why the westward electrojet is modulated strongly by IMF B_y in the winter hemisphere, but only weakly in the summer hemisphere [*Holappa and Mursula*, 2018]. This effect is possibly more significant at dawn than close to midnight, where the auroral oval is less sensitive to seasonal changes in solar irradiation [*Laundal et al.*, 2018].

Considering the modern auroral precipitation models, our results show the importance of the combined effects of IMF B_y and Ψ into future precipitation models. That is, dependence on B_y polarity and Ψ should be added and the two hemispheres should be treated separately. Understandably, current precipitation models combine both hemispheres for the best data coverage [*Newell et al.*, 2014; *Zhu et al.*, 2021]. However, this artificially reduces the B_y dependence and dawn-dusk asymmetries found in this paper. For doing this, it will be important to include all possible particle measurements from different satellites for accurate quantification of B_y dependence in the future models.

5 Conclusions

We used electron precipitation measurements of the DMSP SSJ instruments from years 1995-2022. The data was spatially binned into precipitation maps, and sorted for steady solar wind flow (normalized Newell coupling function $1 < d\Phi/dt/\langle d\Phi/dt\rangle < 2$), positive ($> 2$ nT) and negative (< -2 nT) IMF B_y polarity, and for times of large Earth's dipole tilt angle ($\Psi > 15°$ and $\Psi < -15°$). We showed that for fixed solar wind driving, the IMF B_y and the Earth's dipole tilt angle Ψ together modulate the auroral electron precipitation (1-30 keV) in the following way:

1. The dawn sector precipitation increases for opposite signs of IMF B_y and Ψ at auroral latitudes for energies between 13.9-30 keV in both hemispheres. However, the B_y dependence is more pronounced in the summer hemisphere.

2. In NH summer ($\Psi > 15°$), the auroral precipitation shows a clear B_y dependence for energies 1.4-6.5 keV. Precipitation was found to increase on the dawnside for negative $B_y(< -2$ nT) and on the duskside for positive $B_y(> 2$ nT). This B_y-effect extends to higher latitudes with decreasing energies.

3. In SH summer ($\Psi < -15°$), precipitation was found to increase on the dawnside for positive $B_y(> 2$ nT) and on the duskside for negative $B_y(< -2$ nT), correspondingly.

4. In the summer hemisphere, precipitation patterns of energies 1.4-3 keV exhibit strong dawn-dusk asymmetries, controlled by the sign of IMF B_y.

5. In the NH, the average energy of the precipitation increases on the dawnside for opposite signs of B_y and Ψ.

We also showed that the opposite signs of B_y and Ψ increase the Hall conductance of the NH ionosphere. This B_y effect occurs at slightly higher latitudes in NH summer than in NH winter.

Our results emphasize the need to include the effect of B_y and Ψ in future auroral precipitation models. Thus, more data of auroral precipitation are needed to maintain large enough data coverage after sorting the data by B_y polarity, season, and for separate hemispheres to include the explicit B_y dependence.

Open Research

The DMSP data was downloaded from the CEDAR Madrigal database (`http://cedar.openmadrigal.org`). The solar wind data was downloaded from the OMNI2 database (`http://omniweb.gsfc.nasa.gov/`).

Acknowledgments

We acknowledge the support by the Kvantum Institute of the University of Oulu (ICONIC project). HV was supported by the Academy of Finland project 354521.

References

Anderson, B. J., H. Korth, C. L. Waters, D. L. Green, and P. Stauning (2008), Statistical Birkeland current distributions from magnetic field observations by the Iridium constellation, *Annales Geophysicae*, *26*(3), 671–687, doi:10.5194/angeo-26-671-2008.

Carter, J. A., S. E. Milan, L. J. Paxton, B. J. Anderson, and J. Gjerloev (2020), Height-Integrated Ionospheric Conductances Parameterized By Interplanetary Magnetic Field and Substorm Phase, *Journal of Geophysical Research: Space Physics*, *125*(10), e2020JA028,121, doi:https://doi.org/10.1029/2020JA028121, e2020JA028121 10.1029/2020JA028121.

Chisham, G., M. Lester, S. E. Milan, M. P. Freeman, W. A. Bristow, A. Grocott, K. A. McWilliams, J. M. Ruohoniemi, T. K. Yeoman, P. L. Dyson, R. A. Greenwald, T. Kikuchi, M. Pinnock, J. P. S. Rash, N. Sato, G. J. Sofko, J.-P. Villain, and A. D. M. Walker (2007), A decade of the Super Dual Auroral Radar Network (SuperDARN): scientific achievements, new techniques and future directions, *Surveys in Geophysics*, *28*, 33–109, doi:https://doi.org/10.1007/s10712-007-9017-8.

Cowley, S. (1981), Magnetospheric asymmetries associated with the y-component of the IMF, *Planetary and Space Science*, *29*(1), 79–96, doi: https://doi.org/10.1016/0032-0633(81)90141-0.

Dungey, J. W. (1961), Interplanetary Magnetic Field and the Auroral Zones, *Phys. Rev. Lett.*, *6*, 47–48, doi:10.1103/PhysRevLett.6.47.

Friis-Christensen, E., and J. Wilhjelm (1975), Polar cap currents for different directions of the interplanetary magnetic field in the Y-Z plane, *Journal of Geophysical Research (1896-1977)*, *80*(10), 1248–1260, doi: https://doi.org/10.1029/JA080i010p01248.

Friis-Christensen, E., C. Finlay, M. Hesse, and K. Laundal (2017), Magnetic field perturbations from currents in the dark polar regions during quiet geomagnetic conditions, *Space Science Reviews*, *206*(1-4), 281–297.

Green, D. L., C. L. Waters, B. J. Anderson, and H. Korth (2009), Seasonal and interplanetary magnetic field dependence of the field-aligned currents for both Northern and Southern Hemispheres, *Annales Geophysicae*, *27*(4), 1701–1715, doi:10.5194/angeo-27-1701-2009.

Hardy, D. A., M. S. Gussenhoven, and E. Holeman (1985), A statistical model of auroral electron precipitation, *Journal of Geophysical Research: Space Physics*, *90*(A5), 4229–4248, doi:https://doi.org/10.1029/JA090iA05p04229.

Hardy, D. A., E. G. Holeman, W. J. Burke, L. C. Gentile, and K. H. Bounar (2008), Probability distributions of electron precipitation at high magnetic latitudes, *Journal of Geophysical Research: Space Physics*, *113*(A6), doi: https://doi.org/10.1029/2007JA012746.

Holappa, L., and K. Mursula (2018), Explicit IMF By Dependence in High-Latitude Geomagnetic Activity, *Journal of Geophysical Research: Space Physics*, *123*(6), 4728–4740, doi:https://doi.org/10.1029/2018JA025517.

Holappa, L., T. Asikainen, and K. Mursula (2020), Explicit IMF Dependence in Geomagnetic Activity: Modulation of Precipitating Electrons, *Geophysical Research Letters*, *47*(4), e2019GL086,676, doi:https://doi.org/10.1029/2019GL086676, e2019GL086676 10.1029/2019GL086676.

Holappa, L., R. M. Robinson, A. Pulkkinen, T. Asikainen, and K. Mursula (2021), Explicit IMF By-Dependence in Geomagnetic Activity: Quantifying Ionospheric Electrodynamics, *Journal of Geophysical Research: Space Physics*, *126*(4), e2021JA029,202, doi:https://doi.org/10.1029/2021JA029202, e2021JA029202 2021JA029202.

Korth, H., Y. Zhang, B. J. Anderson, T. Sotirelis, and C. L. Waters (2014), Statistical relationship between large-scale upward field-aligned currents and electron precipitation, *Journal of Geophysical Research: Space Physics*, *119*(8), 6715–6731, doi:https://doi.org/10.1002/2014JA019961.

Laundal, K. M., C. C. Finlay, N. Olsen, and J. P. Reistad (2018), Solar Wind and Seasonal Influence on Ionospheric Currents From Swarm and CHAMP Measurements, *Journal of Geophysical Research: Space Physics*, *123*(5), 4402–4429, doi:https://doi.org/10.1029/2018JA025387.

Li, W., R. M. Thorne, V. Angelopoulos, J. Bortnik, C. M. Cully, B. Ni, O. LeContel, A. Roux, U. Auster, and W. Magnes (2009), Global distribution of whistler-mode chorus waves observed on the THEMIS spacecraft, *Geophysical Research Letters*, *36*(9), doi:https://doi.org/10.1029/2009GL037595.

Li, W., R. M. Thorne, J. Bortnik, Y. Nishimura, V. Angelopoulos, L. Chen, J. P. McFadden, and J. W. Bonnell (2010), Global distributions of suprathermal electrons observed on THEMIS and potential mechanisms for access into the plasmasphere, *Journal of Geophysical Research: Space Physics*, *115*(A12), doi: https://doi.org/10.1029/2010JA015687.

McGranaghan, R., D. J. Knipp, T. Matsuo, H. Godinez, R. J. Redmon, S. C. Solomon, and S. K. Morley (2015), Modes of high-latitude auroral conductance variability derived from DMSP energetic electron precipitation observations: Empirical orthogonal function analysis, *Journal of Geophysical Research: Space Physics*, *120*(12), 11,013–11,031, doi:https://doi.org/10.1002/2015JA021828.

McGranaghan, R. M., J. Ziegler, T. Bloch, S. Hatch, E. Camporeale, K. Lynch, M. Owens, J. Gjerloev, B. Zhang, and S. Skone (2021), Toward a Next Generation Particle Precipitation Model: Mesoscale Prediction Through Machine Learning (a Case Study and Framework for Progress), *Space Weather*, *19*(6), e2020SW002,684, doi:https://doi.org/10.1029/2020SW002684, e2020SW002684 2020SW002684.

Newell, P. T., T. Sotirelis, K. Liou, C.-I. Meng, and F. J. Rich (2007), A nearly universal solar wind-magnetosphere coupling function inferred from 10 magnetospheric state variables, *Journal of Geophysical Research: Space Physics*, *112*(A1), doi:https://doi.org/10.1029/2006JA012015.

Newell, P. T., T. Sotirelis, and S. Wing (2009), Diffuse, monoenergetic, and broadband aurora: The global precipitation budget, *Journal of Geophysical Research: Space Physics*, *114*(A9), doi:https://doi.org/10.1029/2009JA014326.

Newell, P. T., K. Liou, Y. Zhang, T. Sotirelis, L. J. Paxton, and E. J. Mitchell (2014), OVATION Prime-2013: Extension of auroral precipitation model to higher disturbance levels, *Space Weather*, *12*(6), 368–379, doi: https://doi.org/10.1002/2014SW001056.

Ohma, A., J. P. Reistad, and S. M. Hatch (2021), Modulation of Magnetospheric Substorm Frequency: Dipole Tilt and IMF By Effects, *Journal of Geophysical Research: Space Physics*, *126*(3), e2020JA028,856, doi: https://doi.org/10.1029/2020JA028856, e2020JA028856 2020JA028856.

Ohtani, S., S. Wing, P. T. Newell, and T. Higuchi (2010), Locations of night-side precipitation boundaries relative to R2 and R1 currents, *Journal of Geophysical Research: Space Physics*, *115*(A10), doi:https://doi.org/10.1029/2010JA015444.

Redmon, R. J., W. F. Denig, L. M. Kilcommons, and D. J. Knipp (2017), New DMSP database of precipitating auroral electrons and ions, *Journal of Geophysical Research: Space Physics*, *122*(8), 9056–9067, doi: https://doi.org/10.1002/2016JA023339.

Reistad, J. P., K. M. Laundal, A. Ohma, T. Moretto, and S. E. Milan (2020), An Explicit IMF B Dependence on Solar Wind-Magnetosphere Coupling, *Geophysical Research Letters*, *47*(1), e2019GL086,062, doi: https://doi.org/10.1029/2019GL086062, e2019GL086062 10.1029/2019GL086062.

Reistad, J. P., K. M. Laundal, N. Østgaard, A. Ohma, A. G. Burrell, S. M. Hatch, S. Haaland, and E. G. Thomas (2021), Quantifying the Lobe Reconnection Rate During Dominant IMF By Periods and Different Dipole Tilt Orientations, *Journal of Geophysical Research: Space Physics*, *126*(11), e2021JA029,742, doi: https://doi.org/10.1029/2021JA029742, e2021JA029742 2021JA029742.

Robinson, R. M., R. R. Vondrak, K. Miller, T. Dabbs, and D. Hardy (1987), On calculating ionospheric conductances from the flux and energy of precipitating electrons, *Journal of Geophysical Research: Space Physics*, *92*(A3), 2565–2569, doi:https://doi.org/10.1029/JA092iA03p02565.

Sergeev, V., N. Stepanov, Y. Ogawa, S. Käki, and K. Kauristie (2018), Solar wind dependence of electric conductances and currents in the auroral zone, *Journal of Atmospheric and Solar-Terrestrial Physics*, *177*, 38–45, doi: https://doi.org/10.1016/j.jastp.2017.07.006, dynamics of the Sun-Earth System: Recent Observations and Predictions.

Smith, A. R. A., C. D. Beggan, S. Macmillan, and K. A. Whaler (2017), Climatology of the Auroral Electrojets Derived From the Along-Track Gradient of Magnetic Field Intensity Measured by POGO, Magsat, CHAMP, and Swarm, *Space Weather*, *15*(10), 1257–1269, doi:https://doi.org/10.1002/2017SW001675.

Sugino, M., R. Fujii, S. Nozawa, S. C. Buchert, H. J. Opgenoorth, and A. Brekke (2002), Relative contribution of ionospheric conductivity and electric field to ionospheric current, *Journal of Geophysical Research: Space Physics*, *107*(A10), SIA 20–1–SIA 20–15, doi:https://doi.org/10.1029/2001JA007545.

Tenfjord, P., N. Østgaard, K. Snekvik, K. M. Laundal, J. P. Reistad, S. Haaland, and S. E. Milan (2015), How the IMF By induces a By component in the closed magnetosphere and how it leads to asymmetric currents and convection patterns in the two hemispheres, *Journal of Geophysical Research: Space Physics*, *120*(11), 9368–9384, doi:https://doi.org/10.1002/2015JA021579.

Thorne, R. M., B. Ni, X. Tao, R. B. Horne, and N. P. Meredith (2010), Scattering by chorus waves as the dominant cause of diffuse auroral precipitation, *Nature*, *467*(7318), 943–946.

Tsurutani, B. T., and E. J. Smith (1974), Postmidnight chorus: A substorm phenomenon, *Journal of Geophysical Research (1896-1977)*, *79*(1), 118–127, doi: https://doi.org/10.1029/JA079i001p00118.

Weimer, D., and T. Edwards (2021), Testing the electrodynamic method to derive height-integrated ionospheric conductances, *Annales Geophysicae*, *39*(1), 31–51, doi:10.5194/angeo-39-31-2021.

Weimer, D. R. (2001), Maps of ionospheric field-aligned currents as a function of the interplanetary magnetic field derived from dynamics explorer 2 data, *Journal of Geophysical Research: Space Physics*, *106*(A7), 12,889–12,902, doi: https://doi.org/10.1029/2000JA000295.

Wing, S., M. Gkioulidou, J. R. Johnson, P. T. Newell, and C.-P. Wang (2013), Auroral particle precipitation characterized by the substorm cycle, *Journal of Geophysical Research: Space Physics*, *118*(3), 1022–1039, doi: https://doi.org/10.1002/jgra.50160.

Workayehu, A. B., H. Vanhamäki, A. T. Aikio, and S. G. Shepherd (2021), Effect of Interplanetary Magnetic Field on Hemispheric Asymmetry in Ionospheric Horizontal and Field-Aligned Currents During Different Seasons, *Journal of Geophysical Research: Space Physics*, *126*(10), e2021JA029,475, doi: https://doi.org/10.1029/2021JA029475, e2021JA029475 2021JA029475.

Zhu, Q., Y. Deng, A. Maute, L. M. Kilcommons, D. J. Knipp, and M. Hairston (2021), ASHLEY: A New Empirical Model for the High-Latitude Electron Precipitation and Electric Field, *Space Weather*, *19*(5), e2020SW002,671, doi: https://doi.org/10.1029/2020SW002671, e2020SW002671 2020SW002671.